Received: 30 April 2025 | Revised: 11 July 2025 | Accepted: 14 July 2025

DOI: 10.1002/cjce.70061

SPECIAL ISSUE ARTICLE

THE CANADIAN JOURNAL OF CHEMICAL ENGINEERING

Study on iron anchoring methods for magnetic biochar: Characterization, functional mechanism, and RBBR dye removal

Soumik Chakma | **Shrikanta Sutradhar** | **Sudip K. Rakshit** | **Pedram Fatehi** | **Kang Kang**

Biorefining Research Institute (BRI) and Department of Chemical Engineering, Lakehead University, Thunder Bay, Ontario, Canada

Correspondence
Kang Kang, Biorefining Research Institute (BRI) and Department of Chemical Engineering, Lakehead University, Thunder Bay, ON, Canada.
Email: kkang3@lakeheadu.ca

Funding information
Natural Sciences and Engineering Research Council of Canada, Grant/Award Number: RGPIN-2023-03289; Canada Research Chairs, Grant/Award Number: CRC file number 950-231983

Abstract

Magnetic biochar (MBC) is a novel bio-metallic composite material with high potential in sustainable water cleaning. Iron anchoring is critical in forming iron-based MBC and will fundamentally impact its characteristics and functionality in dye removal applications. However, the mechanism is not well-revealed. To understand the iron anchoring mechanism and to identify the most efficient strategy, this study developed and compared three methods for preparing MBC, including impregnation pyrolysis, post-treatment with Fe salts, and one-step co-pyrolysis using maple wood and different types of Fe-containing chemicals, including FeO, $FeSO_4$, and $FeCl_3$, and the products were characterized comprehensively and evaluated for the adsorption of Remazol Brilliant Blue R (RBBR) dye. Key results of this study indicate that the one-step co-pyrolysis method yields the highest adsorption efficiency, with MBC produced at 700°C exhibiting optimal performance. The adsorption capacity of RBBR dye was found to be highest at acidic pH levels, with the 1:1 FeO to biomass ratio achieving a removal efficiency of 100% at a dosage of 0.4 g. Kinetic studies revealed that adsorption follows a pseudo-second-order model, suggesting chemisorption as the primary mechanism. Isotherm analysis indicated that the Langmuir model best describes the adsorption process, with a maximum adsorption capacity of 11.33 mg/g. This study provides new insights into the critical step of iron anchoring design and optimization of MBC synthesis for environmental applications, which could help address growing concerns about water pollution.

KEYWORDS

adsorbent, functional mechanism, magnetic biochar, material characteristics, wastewater treatment

1 | INTRODUCTION

Water pollution remediation has long been a hot spot for research. In recent years, rapid industrialization has led to an alarming increase in the generation of wastewater containing synthetic dyes. The global production of dye exceeds 1,000,000 tons annually due to the increasing consumption of dyes in various industries, including textiles, tanneries, food, cosmetics, and medicine manufacturing.[1] Remazol Brilliant Blue R (RBBR), an anthraquinone-based reactive dye, is extensively used in textile industries due to its vibrant colour. Its discharge into water bodies poses severe environmental and health risks, such as chronic toxicity, surface water discoloration, sunlight disruption, complex treatment, oxygen depletion, metal ion toxicity, and eutrophication.[2] Many methods have been developed to treat dye-containing wastewater, such as membrane filtration, coagulation, flocculation, and so forth.[3–5] However, most of the existing methods either consume expensive chemical reagents or have the problem of high energy consumption.[6,7] Therefore, developing innovative processes that use waste-derived materials and consume less energy to remove dyes is critical.

Adsorption is a promising approach for dye removal from wastewater due to its process simplicity, cost-effectiveness, and high efficiency.[7] Recently, biochar (BC) emerged as an environmentally friendly adsorbent, gaining significant attention due to its cost-effectiveness and good adsorption properties. BC is a carbon-rich porous material that can be produced from many biomass resources, such as wood, agricultural residues, or organic bio-waste, through pyrolysis. Traditionally, BC is produced using woody biomass. However, conventional woody biomass-based BC is very challenging to recycle and reuse, hindering its usability in wastewater treatment. In this regard, incorporating magnetic properties into BC to produce magnetic biochar (MBC) can significantly enhance its recoverability and reusability, further improving its practical applicability in wastewater treatment processes. Specifically, MBC, as a novel type of biomass-based adsorbent, shows high potential for repeatable application, further reducing the quantity required for water cleanup and preventing secondary pollution caused by the dispersion of polluted BC into natural water reservoirs.[8]

Though good progress has been made in using MBC for adsorptive water decontamination, there is a need for more understanding of several critical issues in this field. First, the optimal method for incorporating Fe-containing species into MBC has not been determined. Specifically, it remains unclear whether iron should be impregnated into the biomass before pyrolysis or applied to the BC post-pyrolysis, as these two approaches could lead to varying degrees of adsorption capacity and magnetic properties. Additionally, the influence of different preparation methods on the adsorption efficiency and magnetic performance of the resulting MBC has yet to be systematically studied.[8] Lastly, there is a need to study whether a simplified, one-step co-pyrolysis process can produce MBC with performance characteristics comparable to or superior to those achieved through more complex multi-step approaches, providing more efficient and scalable production. Moreover, there is limited information on how the physicochemical properties of MBC influence its adsorption reaction mechanisms.

To answer the above questions, this study aims to bridge these knowledge gaps by systematically investigating the material characteristics and functioning mechanisms of MBC, with a particular focus on comparing their physicochemical properties resulting from different iron anchoring procedures. By conducting comprehensive analyses, this research will provide new insights into the factors affecting MBC's characteristics and adsorption functionality, identify the most efficient and practical iron anchoring approach, and thus provide valuable information for optimizing the design of MBC for environmental applications.

2 | MATERIALS AND METHODS

2.1 | Materials

Maple wood (MW) chips were obtained from local supply stores in Thunder Bay, Ontario, Canada. Ferrous sulphate ($FeSO_4$), ferric chloride ($FeCl_3$), ferrous oxide (FeO), RBBR dye ($C_{22}H_{16}N_2Na_2O_{11}S_3$), hydrochloric acid (HCl), and sodium hydroxide (NaOH) were purchased from Sigma-Aldrich. Deionized (DI) water was obtained from Nanopure Water, Barnstead. The compressed N_2 gas used for the char preparation was purchased from Linde Canada Inc.

2.2 | Preparation of MBC

MW chips were washed thoroughly with DI water to remove the impurities. They were dried in a constant temperature oven (Model: DKN812, Yamato Scientific) for 48 h at 105°C. The MW chips were downsized using a blade grinder before use. As illustrated in Figure 1, three different methods were used to prepare MBC, including impregnation–pyrolysis (Method 1), post-treatment of BC with Fe salts (Method 2), and direct one-step co-pyrolysis of MW with FeO (Method 3). Detailed explanations on

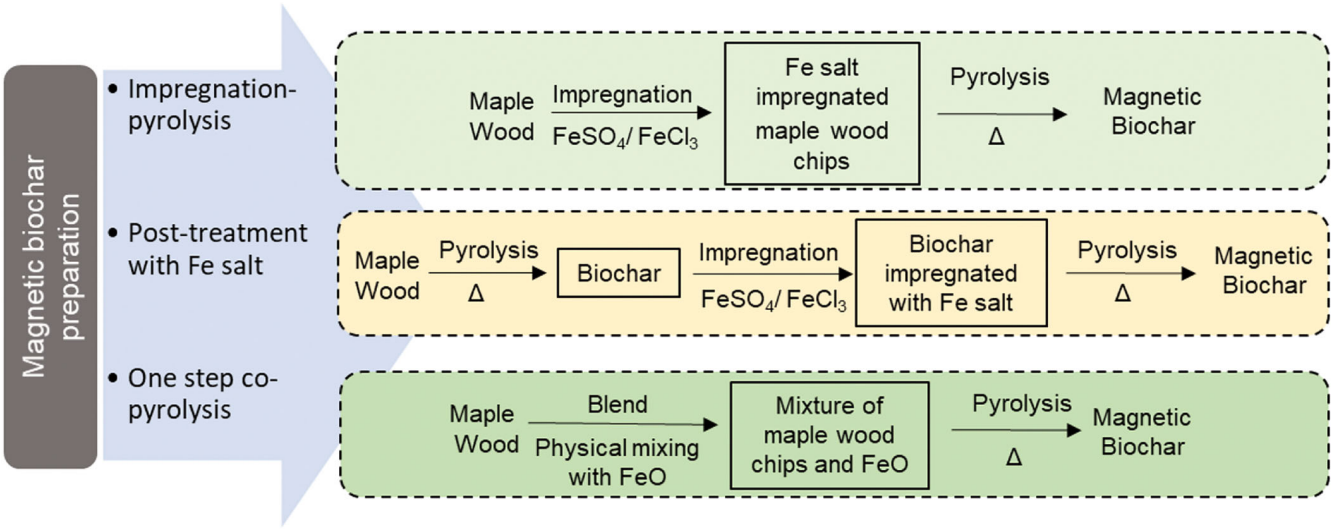

FIGURE 1 Illustration of different iron anchoring procedures of magnetic biochar (MBC) developed and compared in this study.

the preparation methods are presented in the S1 section of the Supplementary Materials. All samples were pyrolyzed in a tube furnace (STF1200-60 × 1000, Across International, USA) at 500–900°C for 3 h under 250 mL/min N_2 flow with a heating rate of 10°C/min. The N_2 flow continued as the furnace cooled to room temperature (approximately 25 ± 2°C) before removing the samples. The pyrolysis conditions for untreated MW chips to produce raw BC were the same as earlier. Afterward, the samples were rinsed multiple times with DI water to remove surface-attached impurities. The samples were then oven-dried at 105°C for 12 h and stored in a container for further characterization. Among these methods, Method 3 (co-pyrolysis) was selected for further experiments based on its superior performance in preliminary tests. The resulting adsorbents from this method were labelled as "*X*:*Y*-MBC, *T*," where "*X*:*Y*" represents the FeO-to-MW mass ratio and "*T*" denotes the pyrolysis temperature. For example, "1:2-MBC700" refers to a sample prepared by co-pyrolysis of a 1:2 FeO-to-MW mixture at 700°C.

The mass yield (%) of the resulting MBC was calculated using the following equation:

$$\text{Yield}\,(\%) = \left(\frac{\text{Mass of char obtained after pyrolysis}}{\text{Initial total mass of FeO} + \text{MW feedstock}}\right) \times 100$$

2.3 | Characterization

Elemental composition (C, H, N, S) was analyzed using a Vario EL Cube elemental analyzer. The proximate analysis (moisture, volatile matter, ash) followed American Society for Testing and Materials (ASTM) standards (ASTM D3173-D3175) using a muffle furnace (Thermolyne, FB1415M, Thermo Scientific, Asheville, USA). Surface morphology and elemental distribution were examined using scanning electron microscopy coupled with energy dispersive X-ray spectroscopy (SEM-EDS) (Hitachi SU-70 Schottky Field Emission SEM, Hitachi, Japan). Functional groups were identified using Fourier transform infrared spectroscopy (FTIR) (Bruker Tensor 37 with ATR), and crystal structures were analyzed via X-ray diffraction (XRD) (PANalytical X'pert Pro) using Cu Kα radiation. X-ray photoelectron spectroscopy (XPS) (Kratos AXIS Supra, Japan) was used for surface chemical state analysis, and data were processed using ESCApe software. Surface area and porosity were evaluated using N_2 adsorption–desorption isotherms using Brunauer–Emmett–Teller (BET) method with a Quantachrome NOVA 2200E after degassing the samples at 150°C for 4 h.

2.3.1 | Magnetic strength test

The magnetic strength of various MBC samples was tested using an "Electricity and Magnetism Kit" by EUDAX (Shenzhen Tianzhiyi Trading Co., Ltd). It was operated at an electric current of 0.5 A. First, the electromagnet was activated and kept on for 2 min. Then, each 0.1 g sample of MBC was placed under the electromagnet. The electromagnet hovered over the MBC samples at a controlled height of 2 mm for 1 min. Then, the sample attached to the device was detached and weighed, and the lifting capacity of the electromagnet was recorded for each sample. The separation efficiency was calculated based on how much the electromagnet could lift the sample. The separation efficiency was calculated using Equation (1).

$$\text{Magnetic separation efficiency} = \frac{\text{Mass of seperated MBC}}{\text{Initial mass of MBC}} \times 100 \quad (1)$$

2.4 | Adsorption capacity, kinetic, and isotherm experiments

The batch adsorption experiment was used to assess the adsorption capacity, kinetics, and isotherm studies. Briefly, 30 mL of RBBR dye solution at varying concentrations (100–500 ppm) was mixed with different adsorbent doses (0.1–1 g) in 50 mL tubes for each test. The adsorption experiments utilized various pH values (3, 5, 7, 9, and 11). 0.1 M HCl or 0.1 M NaOH was used to adjust the sample pH to the required values. The mixtures were shaken at 300 rpm using a shaker (Excella E5, New Brunswick Scientific, Edison, New Jersey, USA) for 2 h. After that, the tubes were removed from the shaker, and the mixtures were filtered using nylon syringe filters (0.2 μm, Sartorius, CA-based). The RBBR dye concentrations in the liquid samples were measured using a Varian Cary 50 Bio UV–visible spectrophotometer at a wavelength of 593 nm. The adsorption capacities of RBBR dye at equilibrium (q_e) were calculated based on Equation (2).

$$q_e = \frac{C_o - C_e}{W} \times V \quad (2)$$

Here, C_o and C_e (mg/L) stand for the initial and final dye concentrations in the liquid phase, respectively; V denotes the volume of the solution (L), and W represents the MBC mass in grams.

Various models were utilized to analyze the adsorption kinetics and isotherms, including pseudo-first-order, pseudo-second-order, intraparticle diffusion model (IPDM), film diffusion model (FDM), Langmuir, Freundlich, and Temkin adsorption isotherms. Detailed explanations of these models are given in Section S2 of the Supplementary Material file.

3 | RESULTS AND DISCUSSION

3.1 | Effect of preparation method on biochar yield and performance

The influence of different preparation methods and pyrolysis temperatures on the physicochemical properties and adsorption capabilities of MBC is demonstrated in Figure S1. Char produced using method 1 exhibited relatively lower dye removal efficiency than the other two methods. This could be attributed to the limited activation of the BC surface due to insufficient impregnation of iron salts and pyrolysis, which results in a less developed porous structure and fewer active sites for adsorption. Additionally, the high temperatures involved in pyrolysis may cause the decomposition of functional groups. On the other hand, methods 2 and 3 demonstrated comparable performance in RBBR dye removal. However, the MBC produced via the direct co-pyrolysis method (method 3) exhibited marginally better efficiency compared to method 2. This improved removal efficiency is likely due to better mixing of FeO with the biomass, which creates more active sites for adsorption. The presence of FeO during co-pyrolysis can act as a catalyst, catalyzing the formation of the carbon matrix and facilitating the protection of functional groups like hydroxyl (—OH) and carboxyl (—COOH) from excessive decomposition. As a result, more adsorption sites are preserved compared to post-treatment methods.

Figure S1B illustrates the influence of pyrolysis temperature (500, 700, and 900°C) on the properties and adsorption performance of MBC. Samples produced at 700 and 900°C exhibited comparable dye removal efficiency, while those prepared at 500°C showed significantly lower performance. The comparable adsorption performance at 700 and 900°C suggests that key structural and chemical properties necessary for dye adsorption were already developed at 700°C, with minimal improvement at higher temperatures. Selvarajoo and Oochit[9] reported that BC produced at 700 and 900°C exhibited similar carbon conversion rates and reduced volatile matter (VM) content compared to those produced at lower temperatures. These findings indicate comparable characteristics, such as reactivity and surface properties, between the two higher-temperature BCs. Given the similar adsorption performance but lower energy input at 700°C, this temperature was selected as the optimal condition for later experiments.

3.2 | Biochar characterization

3.2.1 | Basic properties of non-magnetic and magnetic biochar

Table S1 presents the proximate analysis of MW and its MBC derivatives. All samples showed low moisture content, with 1:1-MBC700 showing the lowest value (0.78%). The low moisture content in MW (1.32%) can be attributed to their naturally lower initial water content, as hardwoods like maple typically retain less moisture than softwoods.[10] MW exhibited high VM content (85.36 ± 0.48%) due to its organic constituents

(cellulose, hemicellulose, lignin). In contrast, MBC samples showed significantly reduced VM, as pyrolysis and the catalytic effect of Fe enhanced thermal decomposition and promoted carbon formation at lower temperatures.[11] Interestingly, higher biomass-to-FeO ratios increase VM content, as reduced FeO content limits catalytic effects, allowing greater retention of volatiles. Ash content also differs notably between samples. MW has very low ash content due to its minimal inorganic components as a woody material. By contrast, MBC samples have higher ash levels, particularly those with higher FeO content. For instance, 1:1-MBC700 exhibited 85.08% of ash, compared to 44.45% in 1:5-MBC700. This difference is attributed to the higher Fe content in 1:1-MBC700, which increases the inorganic fraction remaining after pyrolysis, thereby raising the ash content.[12] Increasing the FeO ratio in MBC significantly alters the proximate characteristics, enhancing thermal decomposition and increasing the ash content due to the higher inorganic load.

The physicochemical properties of the adsorbents are shown in Table 1. Initially, the char yield from co-pyrolysis across all ratios exceeds that of the standard BC sample (22.8%). A notable trend observed among the MBC is that higher FeO to MW ratios result in increased yield, with the 1:1-MBC700 achieving the highest yield of 57.35%. This trend is consistent with findings from other studies.[13] This trend is attributed to the addition of Fe, which will not decompose and lose weight during the pyrolysis process, unlike biomass.[14]

3.2.2 | BET analysis

BET analysis results for MW, BC700, and MBC samples are presented in Table 1. BC700 showed a surface area of 109 m^2/g, pore volume of 0.953 cm^3/g, and a pore diameter of 13.82 Å, indicating a well-developed porous structure suitable for adsorption. Compared to BC700, all MBC samples exhibited lower surface areas due to iron loading. The 1:1-MBC700 had a surface area of 83.37 m^2/g, showing a 23.5% reduction, while 1:2-MBC700 and 1:5-MBC700 had slightly higher values of 87.69 and 86.97 m^2/g, respectively. This reduction is likely due to iron oxide particles blocking some of the pores. In terms of pore volume, MBC samples (0.945–0.952 cm^3/g) remained quite similar to BC700, suggesting that the overall porous structure was mostly retained despite the drop in surface area. However, the average pore diameter significantly decreased in MBCs (1.30–1.35 Å), compared to 13.82 Å in BC700, likely due to partial pore blockage or narrowing caused by iron deposition. This shift toward smaller pores could influence the accessibility and diffusion of larger adsorbate molecules.

3.2.3 | Surface morphology

Figure 2 shows the structural and morphological differences between BC700 and 1:2-MBC700. The SEM image of BC700 (Figure 2A) displays a highly porous structure with a rough surface, formed due to the pyrolysis of MW. EDS analysis confirmed carbon as the major element, along with traces of O, Ca, and K, typical of biomass-derived BC. Compared to BC700, 1:2-MBC700 (Figure 2B,C) retained a similar porous framework but showed increased surface roughness and a higher pore density. These changes are likely due to the incorporation of Fe particles during co-pyrolysis. EDS analysis confirmed the presence of iron in the MBC sample, indicating successful magnetic modification. The deposition of iron oxides also helps explain the reduced surface area observed in BET analysis, likely due to partial pore blockage.

3.2.4 | FTIR analysis

The FTIR spectra in Figure 3A provided the structural changes occurring during the pyrolysis process and the introduction of magnetic properties through co-pyrolysis

TABLE 1 Yield%, surface area, pore volume, and elemental analysis of the adsorbents.

Sample name	Yield (%)	Surface area (m^2/g)	Average pore volume (cm^3/g)	Average pore diameter (Å)	N%	C%	H%	S%	H/C molar ratio
MW	-	-	-	-	16.24	47.54	3.4	0.069	0.86
BC700	22.8	109	0.953	13.82	0.37	90.42	2.78	0.082	0.37
1:1-MBC700	57.35	83.37	0.947	1.3	0.09	16.85	2.3	0.129	1.64
1:2-MBC700	43.75	87.69	0.952	1.32	0.13	29.79	2.14	0.109	0.86
1:5-MBC700	34.94	86.97	0.945	1.35	0.21	48.87	1.9	0.112	0.47

Abbreviation: MW, Maple wood.

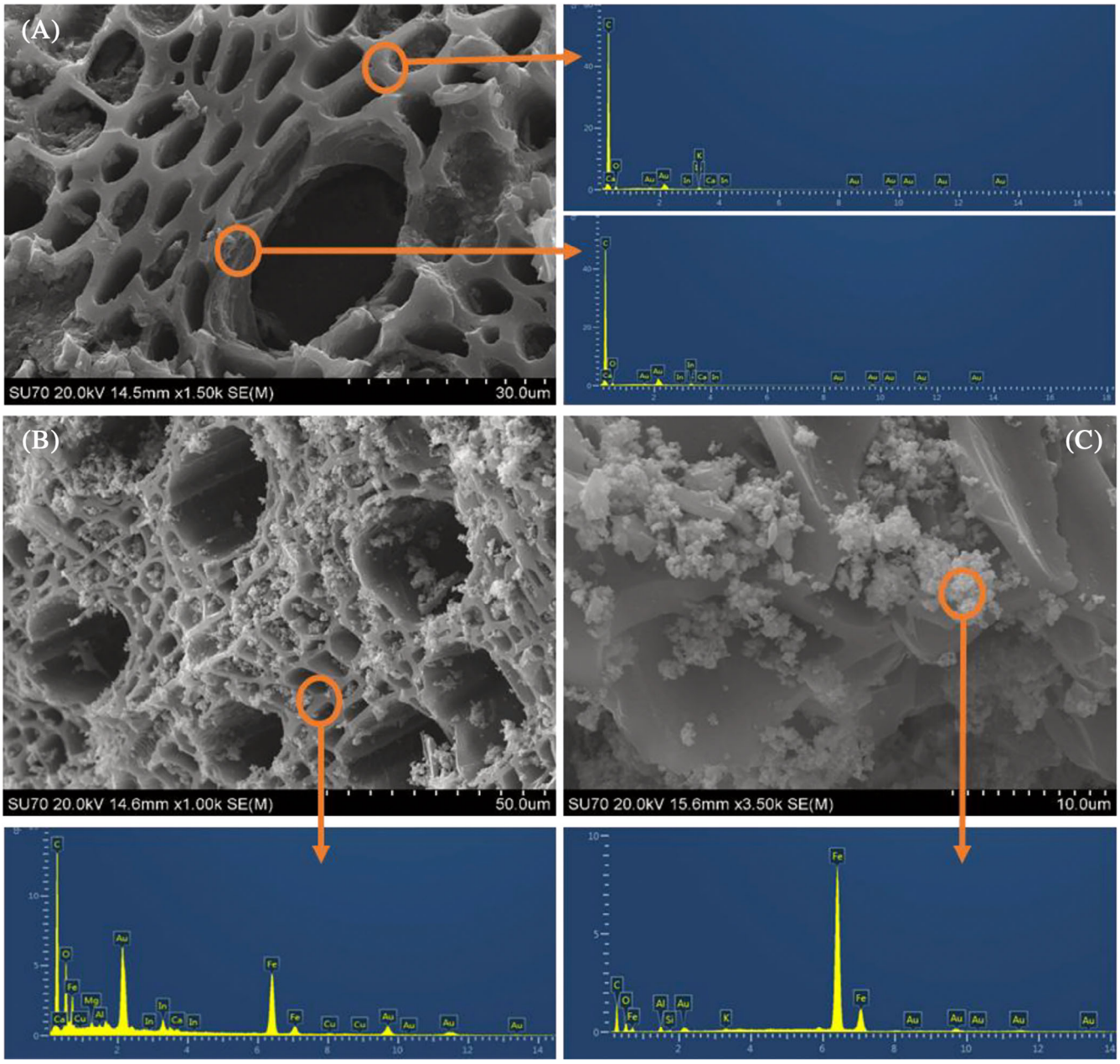

FIGURE 2 Scanning electron microscope (SEM) images of (A) BC700 in 1.50 k magnification, (B) 1:2-MBC700 in 1 k magnification, and (C) 1:2-MBC700 in 3.50 k magnification.

with FeO. The O-H stretching vibrations of hydroxyl groups in cellulose and lignin are observed as a broad peak at 3369 cm^{-1}.[15] A small peak at 2883 cm^{-1} corresponds to the asymmetric stretching vibration of C-H bonds in aliphatic hydrocarbons.[16] Aliphatic hydrocarbons consist of linear or branched chains of carbon atoms bonded to hydrogen atoms. A peak at 1724 cm^{-1} indicates carbonyl (C═O) stretching vibrations due to carboxylic acid groups and C—O stretching vibrations in ester groups.[17] A prominent peak at approximately 1593 cm^{-1} indicates aromatic C═C bonds in lignin structures.[18] A sharp peak at around 1032 cm^{-1} corresponds to C—O stretching vibrations in cellulose and hemicellulose components.[19] Upon pyrolysis, BC and MBC samples exhibited notable changes in their FTIR spectra compared to MW. A small peak was observed in all samples around 3884–3890 cm^{-1}, corresponding to the stretching vibrations of O—H bonds.[20] This peak suggests the presence of —OH groups on the adsorbent surfaces, possibly originating from the decomposition of cellulose and hemicellulose components during pyrolysis. In the case of the MBC samples, distinct peaks were observed around 1510–1514 cm^{-1} and at 903 cm^{-1}. These peaks may be attributed to aromatic C═C bonds and

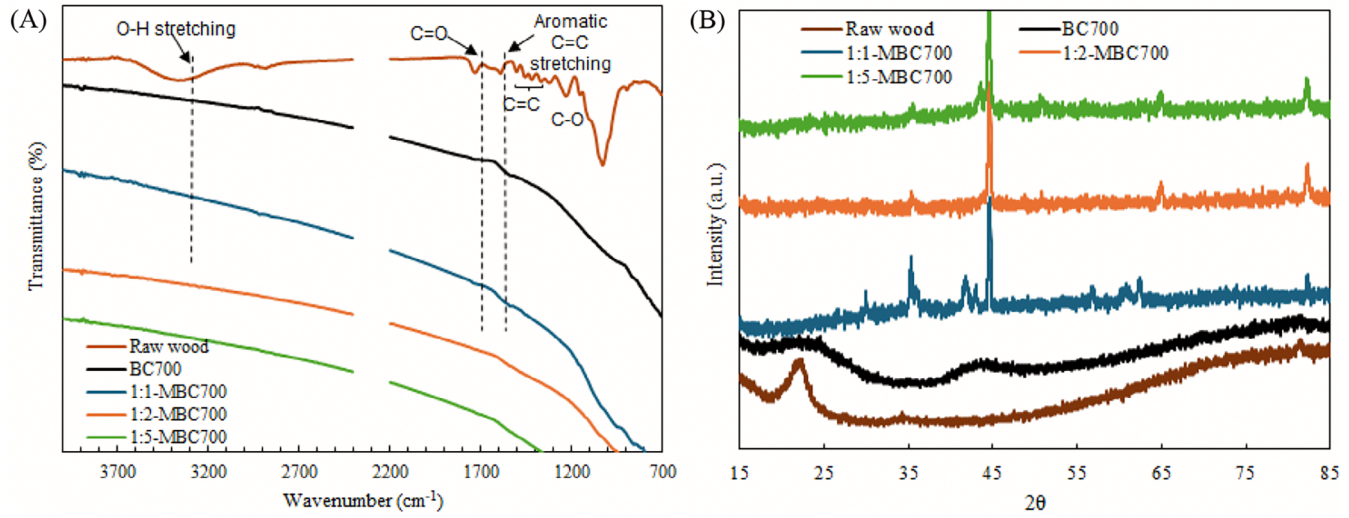

FIGURE 3 (A) Fourier transform infrared spectroscopy (FTIR) and (B) X-ray diffraction (XRD) spectra of Maple wood (MW), BC700, 1:1-MBC700, 1:2-MBC700, and 1:5-MBC700.

Fe—O stretching vibrations, respectively.[21] The appearance of these peaks suggests the successful incorporation of FeO nanoparticles into the BC matrix during co-pyrolysis. This also introduces additional active sites, potentially improving adsorption mechanisms through increased electrostatic interactions, metal ion coordination, and complexation.[22] These FeO nanoparticles can introduce O-H, iron-bound functional groups, which can enhance interactions with RBBR through mechanisms like hydrogen bonding, electrostatic interactions, and complexation, thereby improving the adsorption capacity.[23]

3.2.5 | XRD analysis

In the XRD spectra (Figure 3B), different samples displayed distinct peaks, indicating variations in their crystalline structures and phase compositions. MW showed a distinct peak at approximately 22.5°, indicating the presence of cellulose crystalline structures characteristic of lignocellulosic materials.[24] Upon pyrolysis, the XRD spectrum of BC700 exhibited a small bump at around 22.4°, suggesting the retention of cellulose crystalline structures in the BC matrix. Another slight bump was observed at 44.3°, indicating the (crystal plane of graphite-like structure) amorphous carbonaceous phase resulting from the thermal decomposition of lignin and other organic components. In contrast, the XRD spectra of 1:1-MBC700, 1:2-MBC700, and 1:5-MBC700 revealed notable differences. 1:1-MBC700 exhibited a peak at 30°, which resembles the characteristic of diffraction patterns of Fe_3O_4 or Fe_2O_3, indicating the presence of these iron oxide phases.[25] All the MBC samples showed diffraction peaks at around ~36°, indicating Fe_3O_4, confirming the presence of iron oxide phases.[25] Increasing FeO content in the MBC samples results in sharper, more defined peaks in that region. The peak at approximately 44.5°, associated with the Fe^0 (110) plane, indicates the crystal structures of α-Fe_2O_3 and γ-Fe_2O_3.[26] In the MBC samples, peaks near 63° and 65° indicate the presence of iron oxide phases, such as Fe_3O_4 and Fe_2O_3.[27,28] These peaks suggest the successful incorporation of FeO nanoparticles into the BC matrix during co-pyrolysis, forming MBC. Furthermore, the MBC samples exhibited a small peak at around ~82.4°, which could be attributed to magnetite nanoparticles with a preferred orientation along the (311) crystallographic plane.[13]

3.2.6 | XPS analysis

Figure 4 represents the valence states and chemical compositions of 1:2-MBC700, 1:5-MBC700, and BC700 samples. In Figure 4A, the wide XPS spectra identified carbon (C 1s) and oxygen (O 1s) as the primary elements in both BC and MBC samples, while Fe 2p was the distinct feature for the MBC samples only. In Figure 4B, the O 1s spectra of both samples showed peaks in three regions. These O species include O in C═O at around (530.2~531.7 eV), suggesting the presence of carbonyl groups (C═O)[29] and O-C=O/C-OH at around (532.3~533 eV).[30] The Fe 2p spectra shown in Figure 4C provide insights into the iron species present in the MBC samples. The MBC sample showed Fe $2p_3/_2$ and Fe $2p_1/_2$ peaks at around (710.6~710.9 eV)

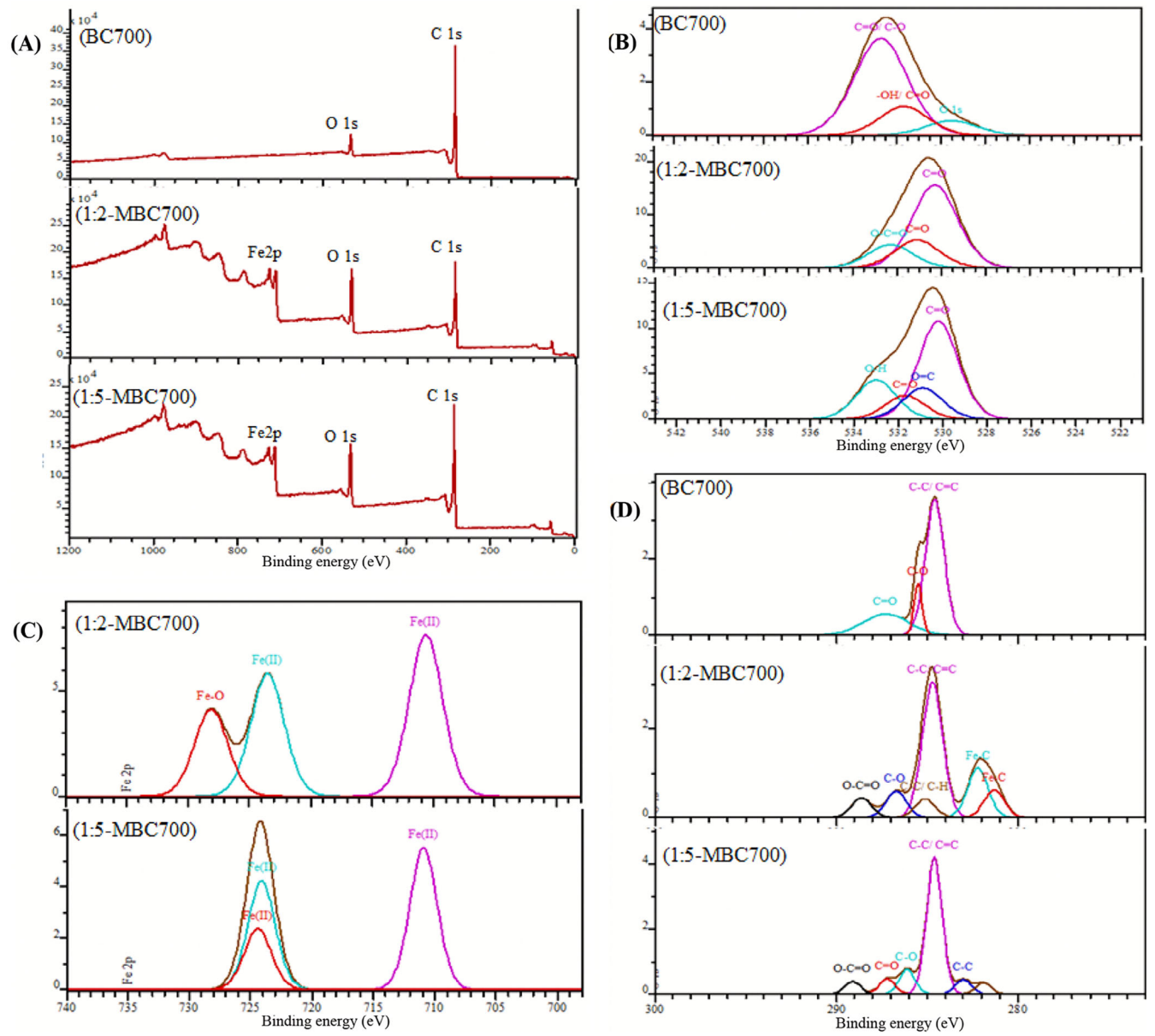

FIGURE 4 X-ray photoelectron spectroscopy (XPS) spectra of BC700, 1:2-MBC700, and 1:5-MBC700 samples: (A) wide scan, (B) O 1s, (C) Fe2p, and (D) C 1s region.

and around (724.1∼724.4 eV) due to the presence of Fe(II) and Fe(III) states of iron in Fe_3O_4 molecule.[31,32] These binding energies indicate the presence of Fe_3O_4, confirming the MBC's magnetic properties.[33] Some satellite peaks are also at around ∼728.1 eV, indicating the Fe^{3+} state.[34,35] In Figure 4D, the C 1s peak for BC showed three peaks, whereas the C 1s peak for MBC showed six distinct components. Those peaks can be fitted into these components: C—C/C═C (graphitic carbon) bonds near 284.6∼284.7 eV, which indicates the presence of aromatic carbon structures[36]; C—O bond near 285.5∼286.1 eV, suggesting hydroxyl (—OH) functionalities on the surface[37]; and C—O or O—C═O bonds near 287.2∼289.1 eV, marking the presence of carboxyl (—COOH) groups that contribute to the surface's acidic sites.[30] The metal–carbide bonds were only observed in the MBC samples at around 281.3∼282.2 eV, signifying interactions between metal components and the carbon matrix.[38]

3.2.7 | Magnetic strength test

Figure S2 shows a clear correlation between FeO content and magnetic separation efficiency. Samples with higher FeO content, like 1:1-MBC700 and 1:2-MBC700, demonstrated the strongest magnetic response and lifting capacity under an electromagnet, due to better alignment of magnetic particles. Preparation temperature also played a key role. MBC produced at 900°C showed the highest

separation efficiency, followed by those at 700°C and 500°C. At 900°C, enhanced thermal decomposition promotes the formation of highly crystalline Fe_3O_4 and Fe_2O_3, improving magnetic strength. MBC prepared at 700°C also showed good magnetic behaviour, with XRD confirming Fe_3O_4 and FeO phases and XPS indicating both Fe^{3+} and Fe^{2+} states. In contrast, MBC synthesized at 500°C likely had incomplete formation of iron oxide phases, resulting in weaker magnetism.

3.3 | Adsorption performance studies

3.3.1 | Impact of adsorbent dosage

All adsorption experiments in this study were conducted using the initial RBBR dye concentration of 100 ppm. As shown in Figure 5A, RBBR removal efficiency increased with adsorbent dosage for all samples. MW had the lowest performance (~28%) due to its unmodified porous structure, while BC700 showed improved efficiency, reaching 55% at 1 g. All MBCs outperformed BC700, particularly 1:1-MBC700 and 1:2-MBC700, showing a similar trend, achieving 100% and 98% removal at 0.4 g, respectively. This superior performance is likely due to the higher FeO content, which increased surface functional groups and active sites.[39] XPS analysis confirmed more —OH and C═O groups, while XRD detected FeO crystalline phases that enhance surface heterogeneity and adsorption. On the other hand, the MBCs with high biomass content (1:3-MBC700 to 1:5-MBC700) showed a similar trend with a relatively lower adsorption efficiency compared to the high Fe-containing MBCs due to fewer magnetic nanoparticles and reduced surface activity.

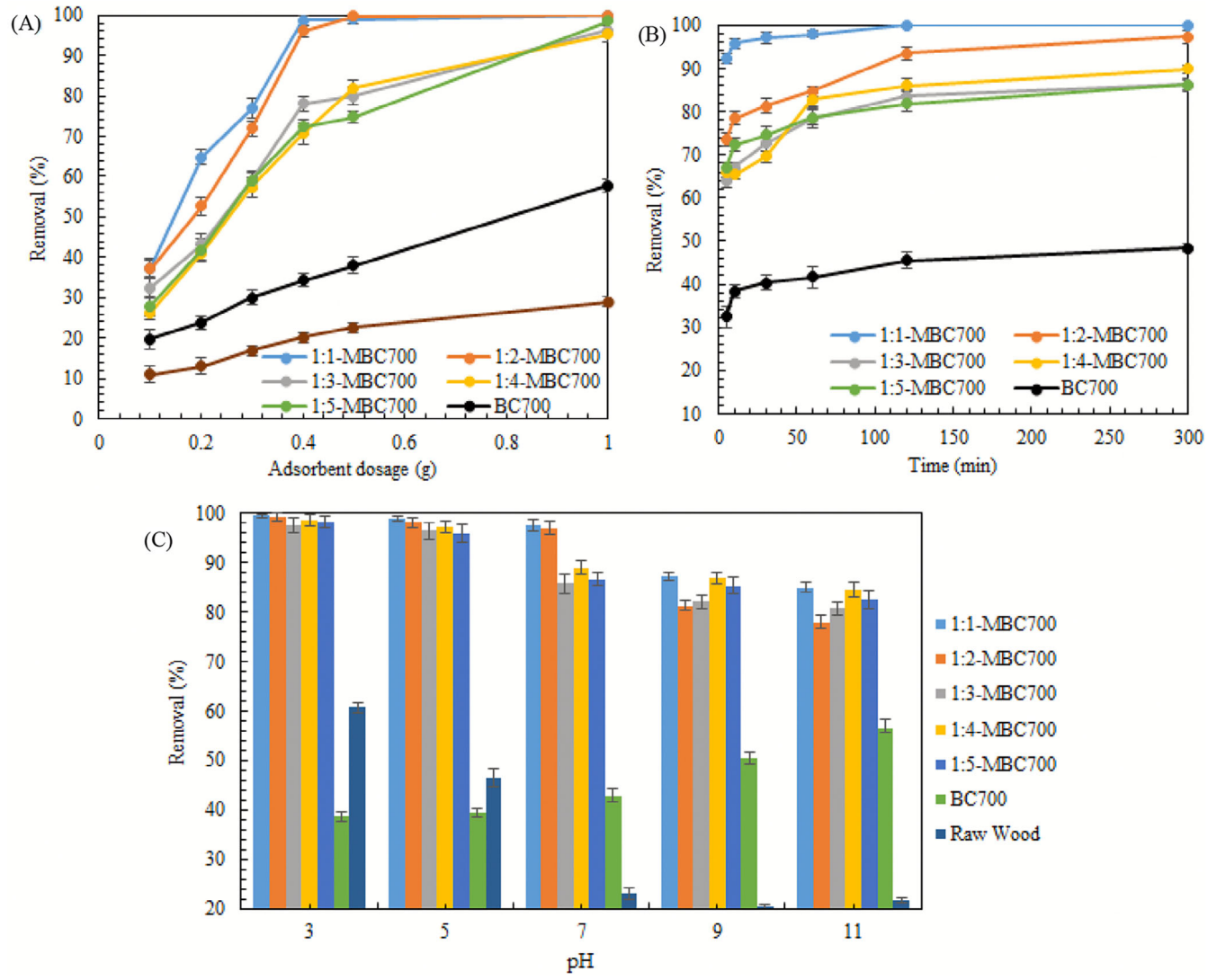

FIGURE 5 Effect of experimental conditions on the removal of 100 ppm Remazol Brilliant Blue R (RBBR) dye: (A) adsorbent dosage (0.1–1 g), (B) contact time (5–300 min), and (C) solution pH (3, 5, 7, 9, and 11).

3.3.2 | Impact of contact time

The impact of contact time was evaluated using 100 ppm RBBR dye with varying adsorption times ranging from 5 to 300 min. As presented in Figure 5B, all samples showed increasing dye removal with time, eventually reaching equilibrium. 1:1-MBC700 showed rapid adsorption compared to the others, reaching equilibrium in less than 5 min of contact time. On the other hand, 1:2-MBC700 took around 120 min to reach equilibrium. In the initial phase, all the adsorbents exhibited rapid dye adsorption, with a significant portion of the RBBR dye being removed within the first 30 min. This is due to the abundant active sites on the BC surface, allowing for swift interaction with adsorbate molecules. During the initial stages of adsorption (from 0 to 30 min), MBC exhibits a substantial available surface area, leading to a rapid biosorption rate.[40] Then, the removal efficiency slowed down over 30 to 300 min. This is because, during this period, the saturation of active sites may occur, limiting further adsorption. After 300 min, equilibrium is reached, where the adsorption rate equals the desorption rate, and the dye removal efficiency stabilizes.

3.3.3 | Effect of pH

The effect of solution pH was examined using 100 ppm RBBR dye, with pH values adjusted from 3 to 11 as shown in Figure 5C. All adsorbents exhibit a consistent trend, showing the highest removal efficiency of more than 97% at pH 3. However, as the solution pH increased, a decrease in the removal efficiency for all adsorbents was observed. The decrease in removal efficiency with increasing pH for the adsorption of RBBR dye by MBC can be attributed to several factors. At lower pH levels, the surface of the MBC becomes positively charged, and the dye molecules may carry a negative charge, facilitating electrostatic attraction and enhancing adsorption.[41] However, as the pH rises, the surface of the MBC becomes more negatively charged due to the deprotonation of acidic functional groups present on the MBC surface. High pH also deprotonates RBBR molecules in the presence of excess OH^- ions, increasing their negative charge. This, coupled with negatively charged dye molecules, decreases the adsorption efficiency.[42]

3.4 | Kinetic studies

This study examined the adsorption kinetics of MBC to evaluate RBBR removal rates from aqueous solutions. The experimental data were fitted to various kinetic models, including the pseudo-first-order (PFOM), pseudo-second-order (PSOM), IPDM, and FDM models, all shown in Figure 6.

The parameters are presented in Tables S2 and S3 in the supplementary file. Across all dye concentrations, the correlation coefficient (R^2) for the PSOM remained consistently high (0.9903–0.9984), surpassing the values for the PFOM (0.688–0.8599), indicating that the PSOM provided a better fit to the experimental data. This observation suggests that the adsorption of RBBR dye onto MBC likely follows chemisorption processes, as has been similarly observed in previous studies of dye adsorption on BC materials[43,44] which also yield adsorption capacities (Q_{cal}) that align closely with the experimental values of Q_{max}, reinforcing the model's applicability. As shown in Table S2, Q_{max} values for RBBR adsorption ranged from 4.84 mg/g at 100 ppm to 21.14 mg/g at 500 ppm, reflecting the concentration-dependent nature of dye uptake by MBC. This trend aligns with the saturation of adsorption sites as the initial concentration increases.[45] Furthermore, the PFOM and PSOM rate constants (k_1 and k_2, respectively) reveal their inverse relationship with RBBR concentration. The PFOM rate constant k_1 decreased from 0.0204 min^{-1} at 100 ppm to 0.0099 min^{-1} at 500 ppm, while the PSOM rate constant k_2 also diminished from 0.1458 g/mg·min at 200 ppm to 0.0099 g/mg·min at 500 ppm. This trend indicates decreased initial adsorption rates at higher concentrations due to the limited availability of active sites, as reported in other studies on BC-based adsorbents.[45] The higher accuracy of the model and the slight decrease in k_2 with increasing concentration suggest that the adsorption of RBBR onto MBC is controlled predominantly by chemical interactions, possibly involving electron-sharing or exchange interactions between RBBR dye molecules and functional groups on the MBC surface, such as hydroxyl (-OH) and carboxyl (-COOH) groups, which facilitate chemisorption.[46,47]

Table S3 shows poor correlation coefficients (R^2) for IPDM, ranging from 0.608 to 0.8475. The non-linearity of the plots suggests that intraparticle diffusion may not be the sole rate-limiting step governing the adsorption process. Instead, it indicates that other mechanisms, such as surface adsorption or film diffusion, might accompany intraparticle diffusion. The correlation coefficients for FDM ranged from 0.6529 to 0.9112. The relatively higher R^2 values compared to the IPDM indicate that film diffusion may play a more significant role in governing the overall adsorption kinetics. This suggests that the transport of dye molecules through the liquid film surrounding the adsorbent particles contributes significantly to the adsorption rate. Compared to all the kinetic models studied, the R^2 values of IPDM and FDM are low compared to the PSOM; the adsorption was mostly chemisorption

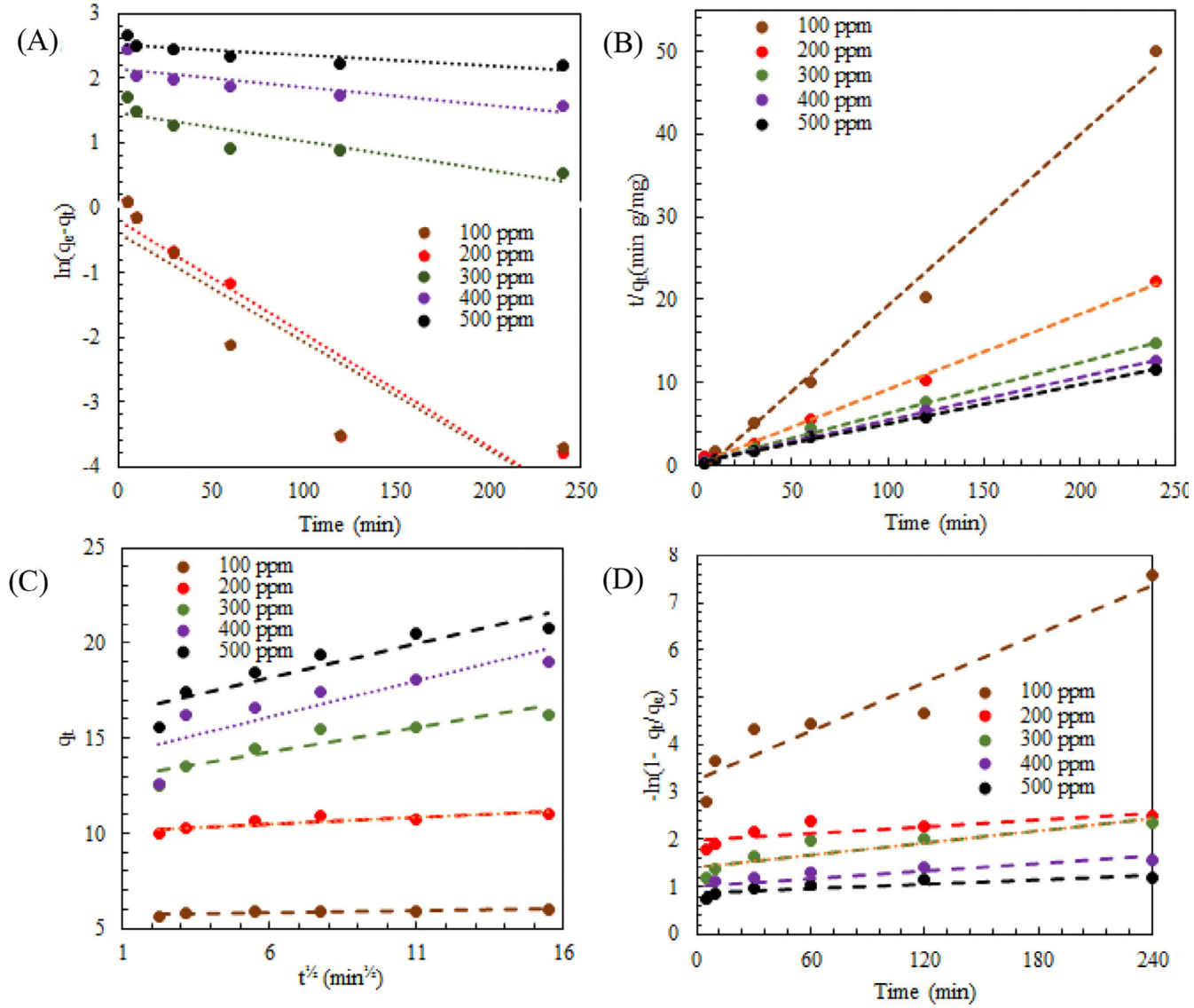

FIGURE 6 (A) Pseudo-first-order (PFOM), (B) pseudo-second-order (PSOM), (C) intraparticle diffusion model (IPDM), and (D) film diffusion model (FDM) of adsorption of Remazol Brilliant Blue R (RBBR) dye by magnetic biochar (MBC) (Dosage = 0.5 g, initial pH = 3.0).

involving sharing or exchanging electrons between the MBC and dye molecules.[48,49]

3.5 | Isotherm studies

The experimental data were analyzed using three common isotherm models: Langmuir isotherm model (LIM), Freundlich isotherm model (FIM), and Temkin isotherm model (TIM), as shown in Figure 7A–C. The corresponding parameters are listed in Table S4.

In Table S4, the R^2 values show that the LIM provided the best fit ($R^2 = 0.9877$) compared to the FIM ($R^2 = 0.9154$) and TIM ($R^2 = 0.925$). This suggests that the adsorption of RBBR dye onto MBC mainly occurs through monolayer adsorption on a surface with uniform adsorption sites. This observation is closely related to the surface chemistry of the MBC. As confirmed by FTIR and XPS analyses, functional groups such as —OH, C═O, and Fe—O were present on the MBC surface, providing specific active sites for dye adsorption. Furthermore, XRD and SEM-EDS analyses revealed a relatively uniform distribution of iron oxide particles, contributing to a more homogeneous surface. These properties favour strong interactions between the dye molecules and the surface sites, consistent with the assumptions of LIM. A higher Langmuir constant ($K_L > 1$) also indicates a strong binding affinity between the MBC and the dye molecules. Similarly, Eltaweil et al.[50] reported that the Langmuir model provided the best fit ($R^2 = 0.998$) for the adsorption of malachite green dye onto MBC derived from corn straw, also attributing it to monolayer adsorption and

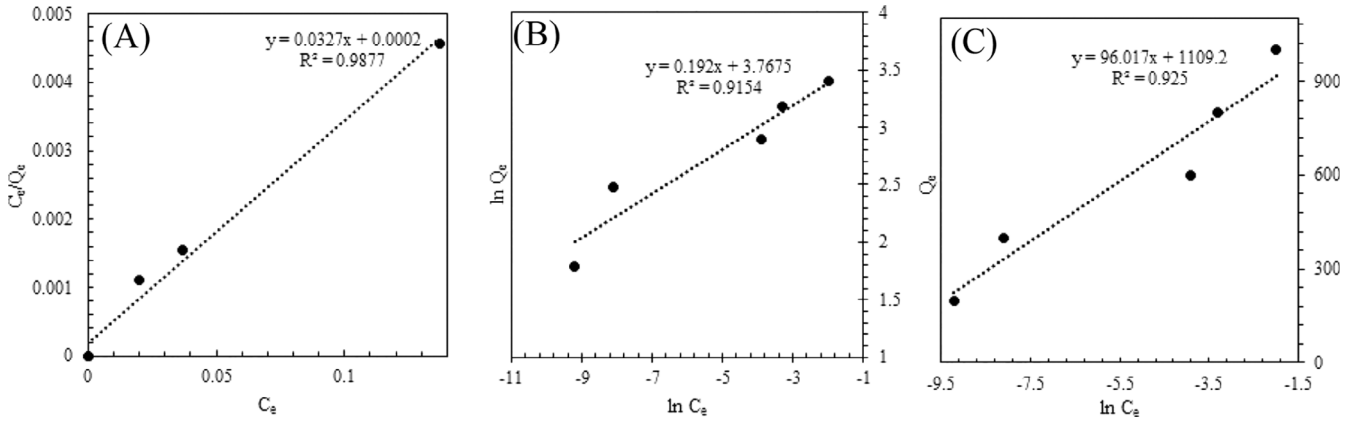

FIGURE 7 (A) Langmuir isotherm model (LIM), (B) Freundlich isotherm model (FIM), and (C) Temkin isotherm model (TIM) profiles for Remazol Brilliant Blue R (RBBR) dye on the prepared magnetic biochar (MBC) (Dosage = 0.5 g, FeO to Maple wood (MW) ratio = 1:2, and initial pH = 3.0).

strong surface interactions. Therefore, the good fit of the LIM in this study reflects the important role of MBC's surface chemistry in facilitating specific, localized monolayer adsorption through mechanisms such as electrostatic attraction, hydrogen bonding, and surface complexation.

The correlation coefficient value ($R^2 = 0.9154$) suggests a reasonable fit of the experimental data to the FIM. It indicates heterogeneous adsorption behaviour and favourable dye adsorption onto the MBC. A lower n_F value (<1) and k_f value of 43.271 from Table S4 indicate relatively low favourability of adsorption and moderate adsorption capacity and affinity between the adsorbate and adsorbent. The TIM showed a correlation coefficient value of $R^2 = 0.925$, indicating a reasonable fit, suggesting that the adsorption process may involve moderate adsorbent-adsorbate interactions and a degree of nonlinearity in the adsorption energy. The Temkin isotherm constant B_T represents the heat of adsorption and reflects the adsorbent–adsorbate interaction energy. A B_t value of 143.47 indicates a relatively strong adsorbent-adsorbate interaction energy. k_t is related to the adsorption equilibrium and indicates the adsorption capacity of the adsorbent material. The k_t value of 12.42 suggests a moderate adsorption capacity and a relatively fast rate.

3.6 | Point of zero charge (pH_{PZC})

The point of zero charge (pH_{PZC}) of the synthesized MBC was determined using the pH drift method, as shown in Figure 8A. The pH_{PZC} was identified at 8.4, meaning that the MBC surface is positively charged at solution pH levels below 8.4, and negatively charged at pH values above this point. Since RBBR is an anionic dye, maintaining the solution pH below the pH_{PZC} led to favourable electrostatic attraction between the positively charged MBC surface and the negatively charged dye molecules, thereby enhancing dye adsorption.

3.7 | Adsorption mechanism

The adsorption of RBBR dye onto MBC occurs via multiple mechanisms, including electrostatic interaction, coordination, surface complexation, π-π stacking, and physisorption, as illustrated in Figure 9. FTIR and XPS analyses confirmed the presence of key functional groups such as —OH, C═O, C—O, C═C, and Fe—O, which facilitate dye binding. Electrostatic attraction plays a significant role, especially at pH levels below the MBC's point of zero charge ($pH_{Pzc} = 8.4$), where the surface is positively charged and effectively attracts the dye's negatively charged sulfonate ($—SO_3^-$) groups.[42] This behaviour is evident in Figure 8B, where strong attraction below pH 8.4 contrasts with repulsion at higher pH. Additionally, Fe atoms in the Fe—O groups on the MBC act as coordination sites, bonding with oxygen atoms in the dye's sulfonic groups, thereby stabilizing the RBBR on the surface. Surface complexation further enhances adsorption, with FTIR and XPS analysis revealing hydroxyl (—OH) and carbonyl (C═O) groups on the adsorbent surfaces. These functional groups interact with the sulfonic and azo groups in the dye through hydrogen bonding, particularly between the —OH groups and the oxygen atoms in the dye's sulfonic groups, strengthening the adsorption process. π-π stacking interactions also play a significant role, as the carbon–carbon double bonds (C═C) in the MBC overlap with the π-electron clouds of the dye's aromatic

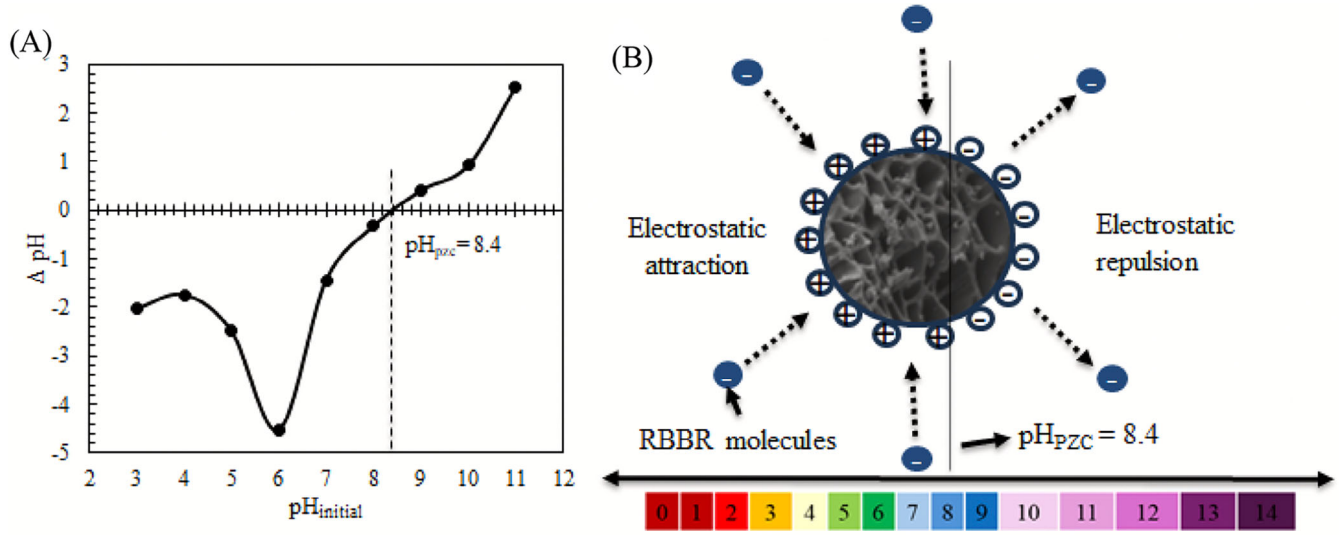

FIGURE 8 (A) Point of zero charge (pH_{pzc}) and (B) influence of surface charge on Remazol Brilliant Blue R (RBBR) adsorption.

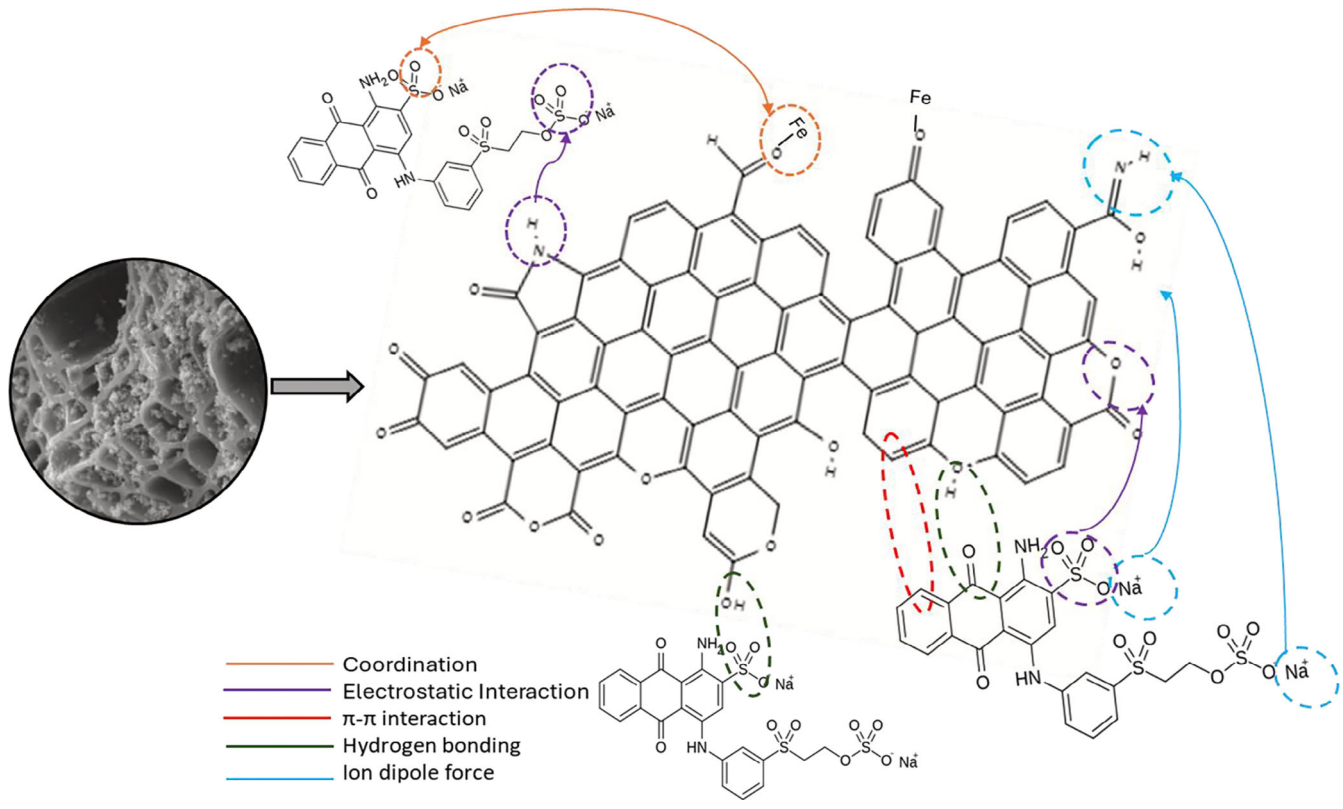

FIGURE 9 Possible adsorption mechanism of Remazol Brilliant Blue R (RBBR) dye onto magnetic biochar (MBC).

rings, stabilizing the dye molecules through non-covalent bonding.[51] Lastly, despite MBC's lower surface area than BC700, its porous structure supports physisorption, allowing dye molecules to diffuse into internal pores after initial surface attachment. These combined mechanisms explain the superior dye removal performance of MBC.

3.8 | Comparison of results from recent studies on dye removal

Table 2 compares recent studies on dye removal using BC-based adsorbents derived from various biomasses, including wood chips, Patula pine wood, mulberry wood waste, southern pine, and beech wood. These studies

TABLE 2 Recent studies on dye removal by various wood-based biochar (BC).

Biomass	Pyrolysis temperature (°C)	Dye	Dye concentration (ppm)	Adsorbent dosage (g/L)	Max. Removal efficiency (%)	Contact time (h)	pH	Reference
Wood chip	Not provided	Acid Blue 161	100	20	93.5	48	7	Ortiz-Monsalve et al.[52]
Patula pine wood	700	Malachite Green	50	6	85.9	1	4	Rubio-Clemente et al.[53]
Mulberry wood waste	500	Methylene Blue	200	200	98	2	9	Mutahir et al.[54]
Southern pine	700	Congo red	300	0.75	98	4	4	Zhang et al.[55]
Beech wood	650	Methylene Blue	20	0.1	100	0.33	6	Zeghioud et al.[56]
Maple wood	700	RBBR	100	16.7	100	2	6.5	This study

demonstrated high dye removal efficiencies, ranging from 85.9% to 100%, with differing pyrolysis temperatures (500–700°C), dye concentrations (20–300 ppm), adsorbent dosages (0.1–200 g/L), contact times (0.33–48 h), and pH levels (4–9). In comparison, this study on MW-derived MBC achieved a maximum removal efficiency of 100% for RBBR dye at a pyrolysis temperature of 700°C, with a dye concentration of 100 ppm, an adsorbent dosage of 16.7 g/L, and a contact time of just 2 h. This study stands out due to its high removal efficiency, relatively moderate adsorbent dosage, and short contact time, demonstrating a more efficient and effective approach for dye removal compared to the other studies.

3.9 | Limitations and future research directions

While this study shows promising results for the removal of RBBR dye using MBC produced from MW and FeO, there are some limitations that should be considered. The experiments were carried out in controlled laboratory settings using a single synthetic dye solution. In real-world applications, wastewater often contains a mix of different pollutants, along with varying pH, salts, and other organic compounds, which could affect the adsorption performance. Additionally, this work focused only on RBBR dye. The effectiveness of the prepared MBC in removing other types of contaminants, such as heavy metals, pharmaceuticals, or other dyes, has not been explored here. Another limitation is that the reusability and regeneration of the MBC were not studied, even though these factors are important for assessing its long-term potential in practical use.

Looking ahead, future research could focus on testing the adsorbent with more complex wastewater samples to better understand how it performs under real conditions. It would also be useful to study the regeneration and reuse of the MBC over multiple cycles to evaluate its stability and cost-effectiveness. Exploring the use of different types of biomass or iron precursors could help improve or tailor the properties of the biochar for specific contaminants. Lastly, investigating the scale-up process and conducting economic assessments would provide helpful insights into whether this material can be realistically applied on a larger, commercial scale.

4 | CONCLUSION

In this study, we successfully synthesized MBC using different iron anchoring methods, with one-step co-pyrolysis proving to be the most effective. The 1:1 FeO-to-biomass ratio, combined with pyrolysis at 700°C, demonstrated optimal adsorption performance for the removal of RBBR dye, achieving a removal efficiency of up to 100%. The study highlights the critical role of iron anchoring in enhancing the physicochemical properties of MBC and its adsorption efficiency. Detailed characterizations revealed the successful integration of magnetic properties and functional groups crucial for adsorption mechanisms, such as chemisorption, hydrogen bonding, and electrostatic interactions. The Langmuir isotherm and pseudo-second-order kinetic models accurately described the adsorption process. This research not only deepens the understanding of MBC synthesis and its functional mechanisms but also offers an energy-efficient method for producing high-performance adsorbents for sustainable water treatment applications.

AUTHOR CONTRIBUTIONS

Soumik Chakma: Writing – original draft; writing – review and editing; visualization; methodology; formal analysis; conceptualization; data curation. **Shrikanta**

Sutradhar: Data curation; methodology; investigation. **Sudip K. Rakshit:** Supervision; funding acquisition; validation; data curation. **Pedram Fatehi:** Resources. **Kang Kang:** Conceptualization; investigation; validation; writing – review and editing; supervision; funding acquisition.

ACKNOWLEDGEMENTS

The authors would like to thank the NSERC (Natural Sciences and Engineering Research Council of Canada) for supporting this study through the Discovery Grant (RGPIN-2023-03289: Kang Kang), Alliance International Catalyst Grants (Kang Kang), and Canada Research Chair Program (Tier 1) in Bioenergy and Biorefining Processes (CRC file number 950-231983: Sudip K. Rakshit).

PEER REVIEW

The peer review history for this article is available at https://www.webofscience.com/api/gateway/wos/peer-review/10.1002/cjce.70061.

DATA AVAILABILITY STATEMENT

The data that support the findings of this study are available on request from the corresponding author. The data are not publicly available due to privacy or ethical restrictions.

ORCID

Pedram Fatehi https://orcid.org/0000-0002-3874-5089
Kang Kang https://orcid.org/0000-0002-7116-549X

REFERENCES

[1] K. Maheshwari, M. Agrawal, A. B. Gupta, in *Novel Materials for Dye-Containing Wastewater Treatment* (Eds: S. S. Muthu, A. Khadir), Springer Singapore, Singapore **2021**, p. 1.
[2] M. Farhan Hanafi, N. Sapawe, *Mater. Today: Proc.* **2020**, *31*, 269.
[3] S. Ihaddaden, D. Aberkane, A. Boukerroui, D. Robert, *Journal of Water Process Engineering* **2022**, *49*, 102952.
[4] H. Rashidi, N. N. Sulaiman, N. Hashim, *Procedia Eng.* **2012**, *44*, 2010.
[5] M. Punzi, B. Mattiasson, M. Jonstrup, *J. Photochem. Photobiol., A* **2012**, *248*, 30.
[6] S. Nannu Shankar, D. R. Dinakaran, D. K. Chandran, G. Mantha, B. Srinivasan, U. P. Nyayiru Kannaian, *Energy Nexus.* **2023**, *10*, 100197.
[7] R. Rashid, I. Shafiq, P. Akhter, M. J. Iqbal, M. Hussain, *Environ. Sci. Pollut. Res.* **2021**, *28*, 9050.
[8] K. Kang, Y. Hu, I. Khan, S. He, P. Fatehi, *Bioresour. Technol.* **2023**, *390*, 129786.
[9] A. Selvarajoo, D. Oochit, *Mater. Sci. Energy Technol.* **2020**, *3*, 575.
[10] V. Stagno, S. Ricci, S. Longo, E. Verticchio, F. Frasca, A. M. Siani, S. Capuani, *Cellulose* **2022**, *29*, 7917.
[11] M.-e. Zhong, G. Tong, J. Sun, N. Zhou, C. Ding, X. Liu, A. Merchant, X. Zhou, *Int. J. Environ. Res. Public Health* **2022**, *19*, 16790.
[12] L. Puri, Y. Hu, G. Naterer, *Front. Fuels* **2024**, *2*, 1378361.
[13] L. Zhang, Y. Dong, J. Liu, C. Liu, W. Liu, H. Lin, *Bioresour. Technol.* **2022**, *347*, 126362.
[14] Y. Wang, Q. Yang, J. Chen, J. Yang, Y. Zhang, Y. Chen, X. Li, W. Du, A. Liang, S.-H. Ho, J.-S. Chang, *J. Hazard. Mater.* **2020**, *395*, 122658.
[15] L. Hu, X.-Y. Wei, X.-H. Guo, H.-P. Lv, G.-H. Wang, *J. Environ. Chem. Eng.* **2021**, *9*, 105859.
[16] M. Kumar, D. Prasad, M. K. Mondal, *Biomass Convers. Biorefin.* **2023**, *13*, 4135.
[17] U. Younis, A. A. Rahi, S. Danish, M. A. Ali, N. Ahmed, R. Datta, S. Fahad, J. Holatko, T. Hammerschmiedt, M. Brtnicky, *PLoS One* **2021**, *16*, e0253390.
[18] C. Zhang, Z. Zhang, L. Zhang, Q. Li, C. Li, G. Chen, S. Zhang, Q. Liu, X. Hu, *Bioresour. Technol.* **2020**, *304*, 123002.
[19] J. Prabahar, B. Vafaei, E. Baffoe, A. Ghahremaninezhad, *Constr. Mater.* **2021**, *2*, 1.
[20] T. C. Egbosiuba, A. S. Abdulkareem, A. S. Kovo, E. A. Afolabi, J. O. Tijani, M. T. Bankole, S. Bo, W. D. Roos, *Sci. Rep.* **2021**, *11*, 75.
[21] E. Leng, Y. He, Y. Xue, L. Leng, H. He, *Ind. Crops Prod.* **2023**, *205*, 117518,
[22] Y. Yi, G. Tu, D. Zhao, P. E. Tsang, Z. Fang, *J. Cleaner Prod.* **2020**, *245*, 118886.
[23] J. Song, Z. Huang, M. Gamal El-Din, *Chem. Eng. J.* **2021**, *421*, 129937.
[24] H. Ezz, M. G. Ibrahim, M. Fujii, M. Nasr, *Biomass Convers. Biorefin.* **2023**, *13*, 10807.
[25] O. Tomin, M. R. Yazdani, *J. Porous Mater.* **2022**, *29*, 849.
[26] S. Mandal, S. Pu, L. Shangguan, S. Liu, H. Ma, S. Adhikari, D. Hou, *Environ. Int.* **2020**, *135*, 105374.
[27] S. Das, S. Mondal, *Environ. Nanotechnol., Monit. Manage.* **2023**, *20*, 100893.
[28] Y. Zhang, N. Liu, Y. Yang, J. Li, S. Wang, J. Lv, R. Tang, *Colloids Surf., A* **2020**, *600*, 124926.
[29] Y. Li, L. Zhu, J. Shi, Y. Dou, S. Li, R. You, S. Zhang, X. Miao, S. Shi, H. Ji, G. Yang, *Appl. Surf. Sci.* **2021**, *561*, 150076.
[30] H. Liang, C. Zhu, S. Ji, P. Kannan, F. Chen, *Biochar* **2022**, *4*, 3.
[31] A. A. H. Saeed, N. Y. Harun, S. Sufian, M. R. Bilad, Z. Y. Zakaria, A. H. Jagaba, A. A. S. Ghaleb, H. G. Mohammed, *Int. J. Environ. Res. Public Health* **2021**, *18*, 7949.
[32] Y. Yi, G. Tu, P. Eric Tsang, Z. Fang, *Chem. Eng. J.* **2020**, *380*, 122518.
[33] F. Meng, Z. Li, C. Lei, K. Yang, D. Lin, *Chem. Eng. J.* **2021**, *413*, 127391.
[34] Y. Wu, L. Xu, J. Shi, J. Cui, S. Han, C. Xia, L. Gan, *Mater. Des.* **2022**, *220*, 110817.
[35] S. T. Neeli, H. Ramsurn, C. Y. Ng, Y. Wang, J. Lu, *J. Environ. Chem. Eng.* **2020**, *8*, 103886.
[36] Y. Chen, R. Ma, X. Pu, X. Fu, X. Ju, M. Arif, X. Yan, J. Qian, Y. Liu, *Chemosphere* **2022**, *308*, 136258.
[37] Z. Chen, Y. Wu, Y. Huang, L. Song, H. Chen, S. Zhu, C. Tang, *Colloids Surf., A* **2022**, *651*, 129728.
[38] N. Zhang, F. Reguyal, S. Praneeth, A. K. Sarmah, *Sci. Total Environ.* **2023**, *886*, 163923.
[39] J. Qu, S. Wang, L. Jin, Y. Liu, R. Yin, Z. Jiang, Y. Tao, J. Huang, Y. Zhang, *Bioresour. Technol.* **2021**, *340*, 125692.

[40] X. Li, C. Wang, J. Tian, J. Liu, G. Chen, *Environ. Res.* **2020**, *186*, 109502.
[41] F. Ullah, G. Ji, M. Irfan, Y. Gao, F. Shafiq, Y. Sun, Q. U. Ain, A. Li, *Environ. Pollut.* **2022**, *314*, 120271.
[42] V. Parimelazhagan, P. Yashwath, D. Arukkani Pushparajan, J. Carpenter, *Int. J. Mol. Sci.* **2022**, *23*, 12484,
[43] P. Ganguly, R. Sarkhel, P. Das, *Surf. Interfaces* **2020**, *20*, 100616.
[44] J. O. Ighalo, K. O. Iwuozor, C. A. Igwegbe, A. G. Adeniyi, *Colloids Surf., A* **2021**, *626*, 127119.
[45] T.-J. Jiang, H. M. Morgan, W.-T. Tsai, H. Chien, T.-B. Yen, Y.-R. Lee, *Sustainability* **2024**, *16*, 6623.
[46] B. Zeng, W. Xu, S. B. Khan, Y. Wang, J. Zhang, J. Yang, X. Su, Z. Lin, *Chemosphere* **2021**, *285*, 131439.
[47] L. Zhu, L. Tong, N. Zhao, X. Wang, X. Yang, Y. Lv, *J. Hazard. Mater.* **2020**, *382*, 121002.
[48] A. Eleryan, M. A. Hassaan, U. O. Aigbe, K. E. Ukhurebor, R. B. Onyancha, M. A. El-Nemr, S. Ragab, I. Hossain, A. El Nemr, *Biomass Convers. Biorefin.* **2024**, *14*, 10599.
[49] H.-O. Chahinez, O. Abdelkader, Y. Leila, H. N. Tran, *Environ. Technol. Innovation* **2020**, *19*, 100872.
[50] A. S. Eltaweil, H. A. Mohamed, E. M. Abd El-Monaem, G. M. El-Subruiti, *Adv. Powder Technol.* **2020**, *31*, 1253.
[51] A. Ahmadi, M. Hajilou, S. Zavari, S. Yaghmaei, *J. Cleaner Prod.* **2023**, *382*, 134967.
[52] S. Ortiz-Monsalve, M. Gutterres, P. Valente, J. Plácido, S. Bustamante-López, D. Kelly, S. L. Kelly, *Bioresour. Bioprocess.* **2020**, *7*, 61.
[53] A. Rubio-Clemente, J. Gutiérrez, H. Henao, A. M. Melo, J. F. Pérez, E. Chica, *J. King Saud Univ., Eng. Sci.* **2023**, *35*, 431.
[54] S. Mutahir, M. A. Khan, H. Ishfaq, S. B. Ahmed, A. S. Abouzied, B. Huwaimel, H. Deng, *Biomass Convers. Biorefin.* **2023**, *14*, 29189.
[55] Z. Zhang, M. Zhang, X. Zhao, J. Cao, *Sep. Purif. Technol.* **2024**, *330*, 125542.
[56] H. Zeghioud, L. Fryda, A. Mahieu, R. Visser, A. Kane, *Materials* **2022**, *15*, 2824.

SUPPORTING INFORMATION

Additional supporting information can be found online in the Supporting Information section at the end of this article.

How to cite this article: S. Chakma, S. Sutradhar, S. K. Rakshit, P. Fatehi, K. Kang, *Can. J. Chem. Eng.* **2025**, 1. https://doi.org/10.1002/cjce.70061